



Development of neural network potential for MD simulation and its application to TiN



Takeru Miyagawa^a, Kazuki Mori^{b,*}, Nobuhiko Kato^b, Akio Yonezu^{a,*}

^a Department of Precision Mechanics, Faculty of Science and Engineering, Chuo University, 1-13-27 Kasuga, Bunkyo-ku, Tokyo 112-8551, Japan

^b Science and Engineering Systems Division, ITOCHU Techno-Solutions Corporation, Kamiyacho Trust Tower, 4-1-1, Toranomon, Minato-ku, Tokyo 105-6950, Japan

ARTICLE INFO

Keywords:

Molecular Dynamics Simulation
Neural Network Potential
Mechanical Property
Titanium Nitride (TiN)

ABSTRACT

Titanium nitride (TiN) is used in various applications because of its excellent wear and corrosion resistance. TiN with a rock-salt-type crystal structure has been investigated extensively, but the existence of non-rock-salt-type phases (e.g., Ti_2N) has only been reported recently from first-principles calculations. Molecular dynamics (MD) simulation is a powerful tool to predict mechanical properties, but it generally requires interatomic potentials. The conventional many-body interatomic potentials (e.g., modified embedded-atom method (MEAM) potential) for rock-salt TiN are not applicable to these other phases. Hence, in this study, a neural network (NN)-based method to create interatomic potentials is developed, which are referred to as neural network potentials (NNPs); hence, MD simulations can be conducted for TiN and other phases. First, ab initio molecular dynamics (AIMD) simulations are conducted to obtain the relationships between atomic configurations and the corresponding total potential energies and forces on each atom. Subsequently, these relationships are used for the NN to generate NNP. NNP can accurately reproduce the energies and forces calculated by AIMD simulations. The mechanical properties of TiN are computed using the NNP and MD simulation and verified with the MEAM potential and its experiment. Finally, MD simulation using the developed NNP is conducted for the other phase (Ti_2N) to investigate its mechanical properties.

1. Introduction

Titanium nitride (TiN) and its derivatives have been used in widespread applications owing to its remarkable properties, including chemical stability, thermal stability, oxidative resistance, good substrate adhesion, high fracture strength, and high hardness [1–5]. The high hardness and corrosion resistance of TiN permits its use as a film or coating on high-speed steel as a cutting tool to improve wear resistance. In addition, TiN is used in semiconductor metallization schemes owing to its high conductivity and diffusion barrier [6]. However, TiN is brittle, i.e., it has relatively low fracture toughness due to excellent resistance to plastic deformation (higher hardness) [7]. Therefore, the improvement of fracture toughness is a critical issue for the deposition of TiN and related materials.

Numerous studies have been conducted on stoichiometric rock-salt TiN and under-stoichiometric $TiNx$ ($0.67 < x < 1.0$) [8]. Several studies have reported phase stability, elasticity, electronic and chemical bonding properties [9,10], and film growth [11,12]. Most studies have focused on stoichiometric rock-salt TiN, while few studies have

investigated non-stoichiometric TiN. Although several metals have numerous nitrides, the existence of other phases of TiN is still unknown. Yu et al. [13] have explored the crystal structures and possible stoichiometries in a Ti-N system by the application of modern computational techniques of the recently developed evolutionary algorithm USPEX [14–16]. TiN was crystallized into the well-known rock-salt structure and the CsCl-type structure [17,18]. In addition, Ti_2N , Ti_3N_4 , and e- Ti_2N_{21} are the possible phases of TiN under normal conditions [19]. A detailed theoretical and computational study of phase equilibria, as well as electronic and mechanical properties of titanium nitrides, at the atomistic scale would provide guidance for the synthesis of these novel crystal structures. As various possible phases and compounds in the Ti-N system make the experimental development of better structures difficult, predictions at the atomistic scale may be an efficient approach with a reliable computational method. Improvements to strength and fracture toughness are critical, which are urgently required for the currently brittle TiN.

Molecular dynamics (MD) simulation is a powerful tool to understand physical properties at the atomic scale, which permits the

* Corresponding Author.

E-mail addresses: kazuki.mori.013@ctc-g.co.jp (K. Mori), yonezu@mech.chuo-u.ac.jp (A. Yonezu).

prediction of physical performance with respect to the atomistic structure. Brittleness and sensitivity to crack propagation results from local deformation around a small defect. Thus, the mechanism of local deformation toward fracture must be understood to reduce brittleness. Hence, MD simulation is expected to reveal the deformation process of crystal structures and provide guidelines to improve mechanical performance (especially fracture toughness) of the atomistic structure. However, owing to a complex stoichiometry and its structure in the Ti-N system, interatomic potentials may be lacking for MD simulation. In general, the development of interatomic potentials requires considerable effort as ab initio calculations and numerous fittings of the theoretical function are required. In other words, the existence of empirical interatomic potentials of target materials is a critical issue. A bottleneck of MD simulation of the Ti-N system is the lack of reliable interatomic potentials. Although ab initio calculations can render high accuracy of interatomic interactions for the Ti-N system [13,20], they are limited to several hundred atoms and within a few hundred picoseconds (ps) of simulation time. Therefore, MD simulations are beneficial for investigating long-term phenomena and larger scales, which is key to understanding mechanical properties. Thus, the case with no interatomic potentials leads to a critical limitation to discovering and improving the material and understanding the atomistic mechanism via MD simulation.

The development of condensed matter interatomic potentials using machine learning was first proposed by Behler and Parrinello [21], and subsequently applied to MD simulations in several studies [22–25]. Based on these previous studies, deep learning methods with deep neural network (DNN) models of many-body atomic interactions [26–28] have been developed recently to overcome the dilemma of simulation speed and accuracy. In a recently developed NN learning software package called DeePMD-kit [29], snapshots (which include the total potential energies, forces on each atom, and virial for a set of atomic configurations) from ab initio calculations were prepared and used to train a DNN model for interatomic potentials. After the training process, the trained DNN models were used in MD simulations, which not only accurately reproduced the potential energy and force of the training dataset but also accurately predicted the structural and mechanical properties of the model materials. Moreover, the interatomic potentials constructed using the trained DNN models are applicable in the standard LAMMPS package [30] to run MD simulations. Tang et al. [31] have developed an interatomic potential for Al-rich Al-Tb alloys by using the DNN learning method. The potential energies and forces in the training dataset were calculated by first-principles density functional theory (DFT) using VASP [32,33]. They demonstrated that the DNN interatomic potentials more accurately describe the structures of Al90Tb10 liquid/glass and various Al-Tb crystalline phases compared with those from ab initio calculations and experiments. Such frameworks may be beneficial for other material systems including TiN, which is of interest in this study.

Therefore, in this study, an interatomic potential for the Ti-N system using a DNN is developed. The phases of a Ti-N system are well known to include Ti_3N_2 , Ti_4N_3 , Ti_6N_5 , Ti_2N , and TiN_2 , which are candidate compounds. Among these, Ti_2N can be synthesized by the plasma process, which may have practical applications. A previous study investigated Ti_2N and reported that it may be suitable as the anode material in lithium-ion batteries [34]. A reliable interatomic potential of TiN is already published as a modified embedded-atom method (MEAM) potential [35]. However, to our best knowledge, other compounds do not exist. Thus, a reliable interatomic potential for TiN system is required for MD simulation. In Section 2, the DNN learning method for interatomic potentials is described. In Section 3, the details of dataset generation for training the DNN model and the parameters of the DNN learning process are discussed. In Section 4, the reliability of the DNN interatomic potential is demonstrated. In Section 5, MD simulations of TiN are conducted to investigate deformation behavior during tensile loading and crack propagation and to evaluate mechanical properties including

fracture toughness. Next, the results of MD simulation using the developed DNN potential against those using the conventional MEAM potential are compared to mechanically verify our developed potential. In addition, the computed fracture toughness is compared with experimental data to verify the MD simulations. Finally, various MD simulations including TiN and its related compound (Ti_2N) are conducted to explore materials with better mechanical properties. In Section 6, a summary and conclusions are presented.

2. Interatomic potential via the DNN learning method

2.1. Details of NN

Artificial neural networks (ANNs) provide a precise tool for specific functions. NNs comprise conjugated layers of nodes, separated into three layers: input, output, and hidden layers. The input layers collect input data. The output layers produce results for the given inputs. The hidden layers perform computations and contain parameters that are optimized by minimizing the loss function.

The interatomic potential is developed by passing a set of descriptors to the input layer of the NN. These descriptors $\{D_i\}$ include the atomistic local environment around every atom i of the structure in training dataset. The energy E_i of each atom is extracted from the output layer. The total potential energy E of each structure can be calculated as the sum of each atomic energy E_i i.e., $E = \sum_i E_i$. The mapping from descriptors to each atomic energy E_i is performed by hidden layers in the NN [21,26]. The hidden layers consist of different nodes, where the connection weights between nodes in different layers and bias parameters of each node map the relationships between descriptors and energy. These connection weights and biases are optimized by minimizing the loss function on the training dataset. Thus, the potential energy surface is determined once the weights and parameters in the NN are optimized and fixed by the training process. Moreover, the forces on each atom can be extracted from the potential energy represented by the NN. Fig. 1 shows an illustration of the NN that map descriptors to energy.

The DeePMD-kit software package was used to train the DNN interatomic potentials [29]. A critical step to model interatomic potentials by a DNN is the creation of local structure descriptors $\{D_i\}$ from the Cartesian coordinates of input atomistic structures. The descriptors $\{D_i\}$ must satisfy the constant condition to ensure invariance of the total energy regarding the translation or rotation of the structures or the interchange of two atoms of the same element in the structure. The local coordinate frame developed in the DeePMD-kit was used to construct descriptors $\{D_i\}$. These descriptors $\{D_i\}$ were constructed in two steps. First, the Cartesian coordinates $\{R_i\}$ of the neighboring atom j within the cutoff radius r_c of atom i were changed to the generalized coordination $\{\hat{R}_i\}$, which is defined as follows:

$$\{R_i\} = \{x_{ji}, y_{ji}, z_{ji}\} \rightarrow \{\hat{R}_i\} = \{s(r_{ji}), \hat{x}_{ji}, \hat{y}_{ji}, \hat{z}_{ji}\} \quad (1)$$

where $\hat{x}_{ji} = s(r_{ji})x_{ji}/r_{ji}$, $\hat{y}_{ji} = s(r_{ji})y_{ji}/r_{ji}$, and $\hat{z}_{ji} = s(r_{ji})z_{ji}/r_{ji}$. The function $s(r_{ji})$ is defined as follows:

$$s(r_{ji}) = \begin{cases} \frac{1}{r_{ji}}, & r_{ji} < r_{cs} \\ \frac{1}{r_{ji}} \left\{ \frac{1}{2} \cos \left[\pi \frac{r_{ji} - r_{cs}}{r_c - r_{cs}} \right] + \frac{1}{2} \right\}, & r_{cs} < r_{ji} < r_c \\ 0, & r_{ji} > r_c \end{cases} \quad (2)$$

where r_{cs} is the smooth cutoff parameter. In the next step, an embedding NN is introduced, in which the only input is the radial information $s(r_{ji})$. This NN is called the filter NN (Fig. 1). The outputs of the filter NN are weight coefficients for the structure descriptors $\{D_i\}$ that describe atomistic information around atom i . Then, $\{D_i\}$ is input into another

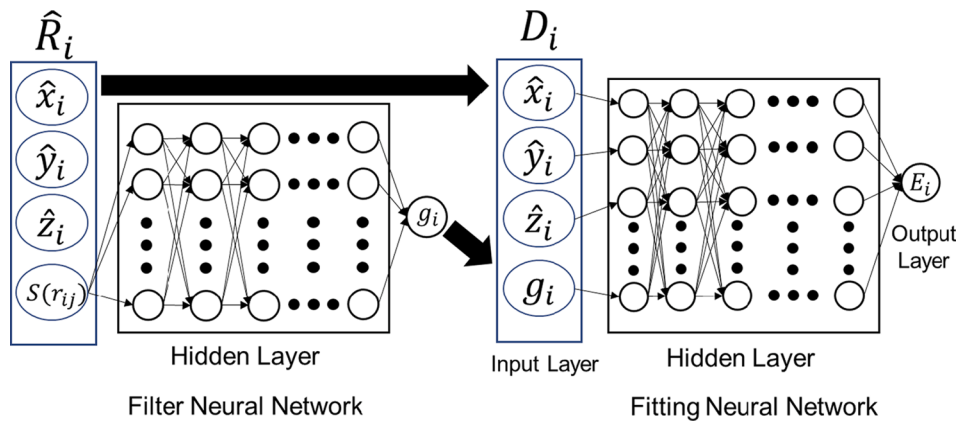


Fig. 1. Structure of the NN.

NN, called the fitting NN, affording atomic energy E_i . Therefore, the local structure is mapped to atomic energy.

2.2. Training data preparation and the training process

Fig. 2 shows the flowchart for modeling the interatomic potential by the NN, i.e., neural network potential (NNP). The accuracy and reliability of NNP are determined by its training process and training data. Thus, the preparation of training data is critical for accurate MD simulations. CALPHAD software Thermo-Calc 2021b [36] and TCTI3 were used to calculate the phase diagram of TiN (Fig. 3). Fig. 3 shows that TiN exists at a wide range of temperatures of up to 2,500 °C, with a nitrogen content of 30–50%. Ti_2N also exists at a wide range of temperatures of up to 1,000 °C, with a nitrogen content of 5–45%. Hence, it is worthy to create the interatomic potential of Ti_2N for MD simulation.

The aim of our NNP is to simulate TiN and Ti_2N in MD. Hence, TiN and Ti_2N datasets were prepared separately, and both datasets were composed of snapshots obtained by ab initio molecular dynamics (AIMD) simulation. All AIMD simulations were conducted by using the VASP package [32,33]. Some of the simulations were performed using the Exabyte.io platform, which is a web-based computational ecosystem for the development of new materials and chemicals [37]. The timestep for AIMD simulations was set to 0.5 fs, and an NPT ensemble with a Langevin thermostat was applied in all simulations. The projector-augmented-wave (PAW) method was applied to describe the core-

valence electron interaction. For the exchange–correlation potential, the generalized gradient approximation (GGA) in the Perdew–Burke–Ernzerhof form was used. Only the gamma point was used to sample the Brillouin zone, and the default energy cutoff for the plane wave basis set from the PBE potential was used.

For the TiN dataset, AIMD simulations were performed with a cubic cell containing 32 Ti atoms and 32 N atoms with periodic boundary conditions. Two structures of TiN were prepared for AIMD simulations, i.e., stoichiometric rock-salt TiN and amorphous TiN, respectively, to precisely simulate the movement of atoms of classical MD simulations in AIMD. The amorphous TiN structure was created by heating the rock-salt TiN structure at 16,000 K with an NVT ensemble and a Langevin thermostat. Then, the following AIMD simulation was applied to the rock-salt and amorphous structures. The simulation temperatures of rock-salt TiN structures were 300, 500, 1,000, 2,000, 3,000, and 4,000 K, while the simulation pressures were –50, –10, 0, 1, 10, and 50 bar. For amorphous TiN simulations, simulation temperatures were 1,000, 2,000, 3,000, and 4,000 K, while simulation pressures were –50, –10, 0, 1, 10, and 50 bar. The total simulation times for rock-salt TiN and amorphous TiN were 250 fs and 500 fs, respectively. Thus, 500 snapshots of data on the total energy and force on each atom are collected for each rock-salt TiN structure, while 1,000 snapshots of data for each amorphous TiN structure are collected. Overall, about 42,000 snapshots were collected for the TiN dataset and used to train the DNN.

In addition, a Ti_2N dataset was also prepared. The simulation model

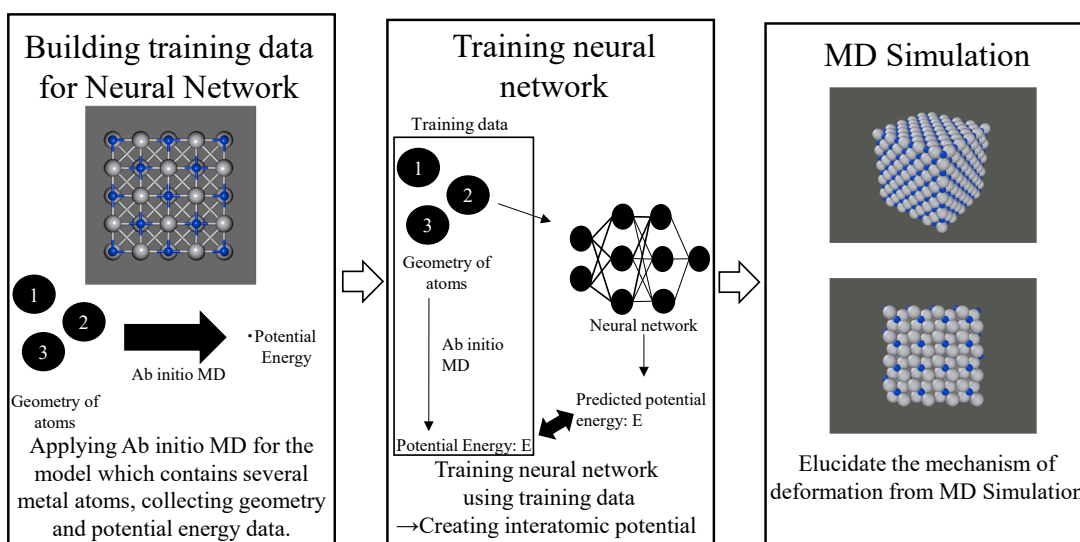


Fig. 2. Schematic flowchart for modeling the interatomic potential by the NN.

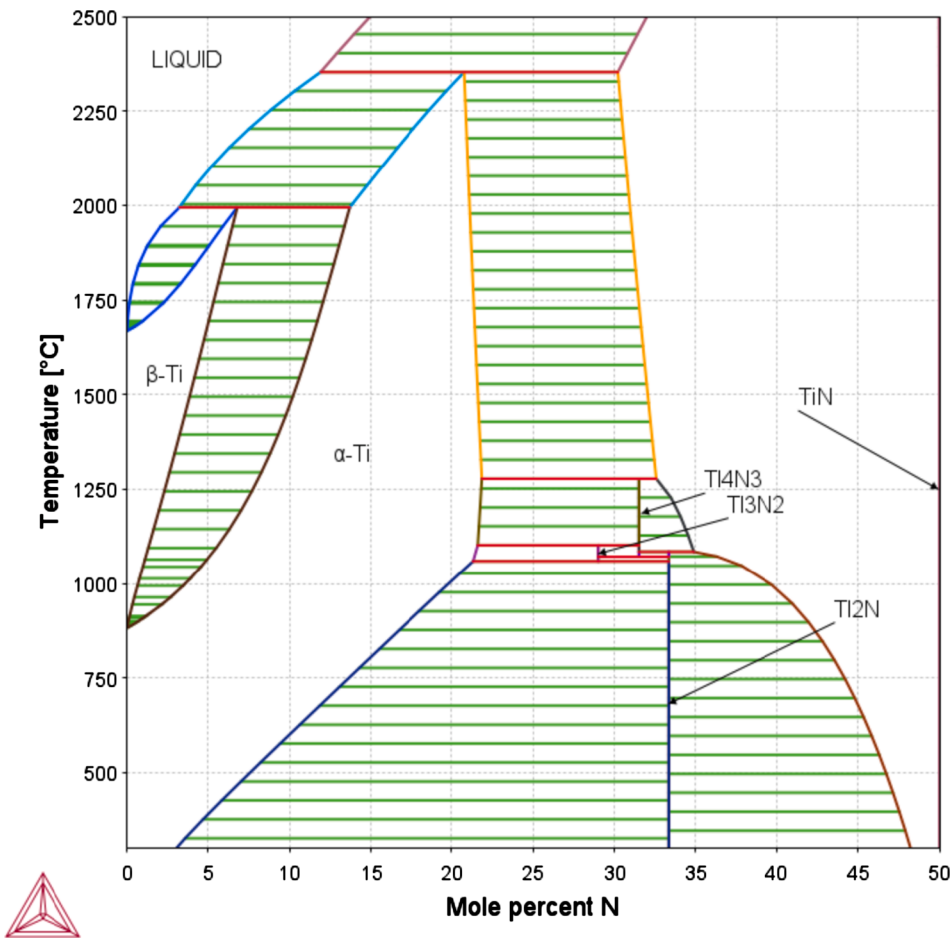


Fig. 3. Titanium-nitrogen binary phase diagram.

comprised 108 Ti atoms and 54 N atoms. Two structures of Ti₂N were prepared for AIMD simulations, i.e., crystalline Ti₂N (P42/mnm) and amorphous Ti₂N, respectively, to predict atomic motion and trajectories in classical MD simulations. The amorphous Ti₂N structure was prepared by heating crystalline Ti₂N at 16,000 K in AIMD with an NVT ensemble and the Langevin thermostat. The simulation temperatures of crystalline Ti₂N were 300, 500, 1,000, 2,000, 3,000, and 4,000 K, and the pressures were -50, -10, 0, 1, 10, and 50 bar. For amorphous Ti₂N, the simulation temperatures were 1000, 2000, 3000, and 4000 K, and the pressures were -50, -10, 0, 1, 10, and 50 bar. The total simulation time was 500 fs for crystalline Ti₂N, and 1,000 fs for amorphous Ti₂N. Overall, 1,000 snapshots of data on the total energy and force on each atom were collected for each crystalline Ti₂N structure, and 2,000 snapshots for

amorphous Ti₂N were collected. The Ti₂N dataset consisted of 84,000 snapshots and was used to train the DNN.

3. Performance of the DNN interatomic potential

3.1. Potential energy and interatomic force

Fig. 4 and **Fig. 5** show the comparison of the energies and interatomic forces predicted by the optimized NN to the test data created by AIMD. **Fig. 4** and **Fig. 5** show the results for TiN and Ti₂N, respectively. The simulation temperatures were 750 K and 1,500 K, while the pressure was set to 0 bar, which was not included in the training data. The vertical axis denotes the energies or forces of snapshots predicted by the NN, and

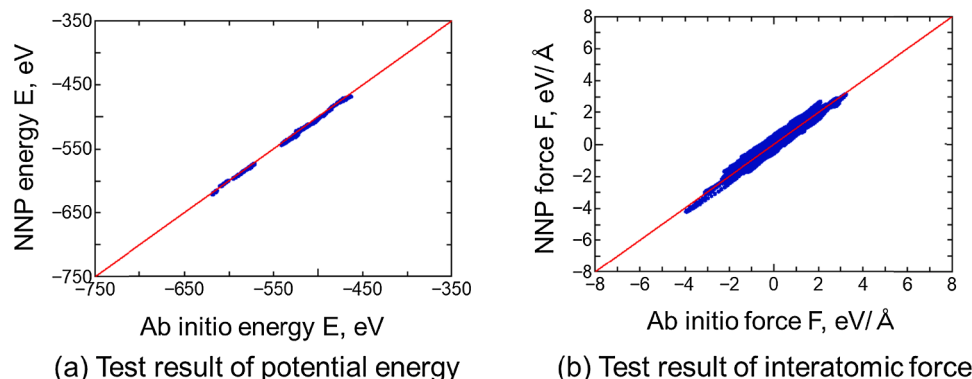
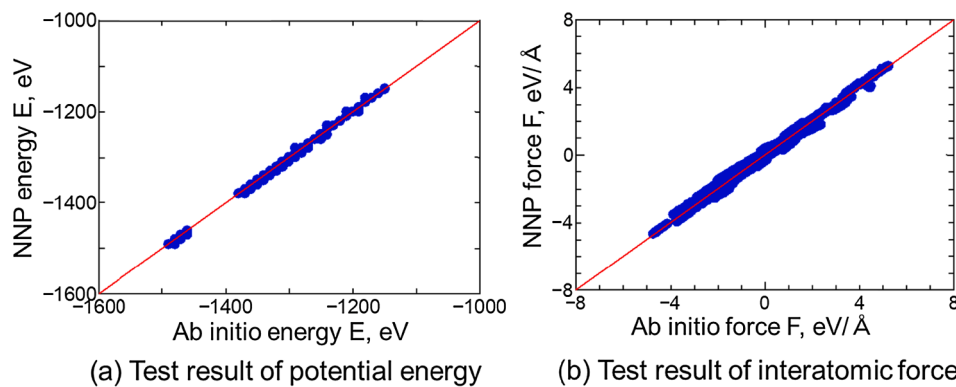


Fig. 4. Test results of the NN for TiN.

Fig. 5. Test results of the NN for Ti_2N .

the horizontal axis represents the energies and forces from ab initio calculations. For the TiN system, the root-mean square error (RMSE) of energy was 1.06 meV per atom and the force RMSE was $0.10 \text{ eV}\text{\AA}^{-1}$ for the training data. This was sufficient to predict the energy and force based on the coordinates of structures. Moreover, the test data RMSE was 6.06 meV of energy per atom and $0.27 \text{ eV}\text{\AA}^{-1}$ for force. The trained NN could accurately reproduce the energy and force for the atomic configurations in training data, as well as for the structures in the test data.

For the Ti_2N system, the training RMSE was 7.53 meV of energy per atom and $2.20 \text{ eV}\text{\AA}^{-1}$ for force. The test RMSE was 5.14 meV of energy per atom and $1.48 \text{ eV}\text{\AA}^{-1}$ for force. These results also indicated that the trained NN for the Ti_2N system could accurately reproduce the energy and force for the training and test data.

3.2. Calculated material properties (lattice constant, elastic constants, and coefficient of thermal expansion)

Various properties obtained from the NNP and ab initio calculations for TiN and Ti_2N were compared to verify the developed NNP. For NNP, all simulations were conducted using the LAMMPS package [30].

Table 1 shows the lattice constants, elastic constants, Poisson's ratio, Young's modulus, shear modulus, and bulk modulus of TiN and Ti_2N for the comparison of NNP and ab initio calculations. For TiN, the MEAM potential was created from a previous study [35]; hence, the MEAM potential and NNP are compared. The NNP of TiN and Ti_2N predicted each lattice constant very accurately. Hence, NNP can reproduce the energy and force based on input structures, as well as more practical properties (Table 1). Although some elastic constants were predicted

less accurately by NNP, most were predicted with some precision. These inaccuracies resulted from the precision of the training data. As numerous structures were needed to develop the NNP of TiN and Ti_2N , only gamma points were used to sample the Brillouin zone due to longer computational times, which reduced the accuracy of some properties.

For TiN, coefficients of linear thermal expansion were reported [39]. The coefficients of linear thermal expansion from the NNP and experiments were compared. Fig. 6 shows the relationship between temperature and change of cell length. The coefficient of linear thermal expansion α_L was calculated as follows:

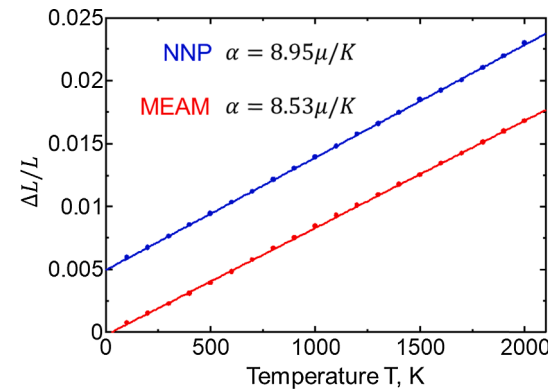


Fig. 6. Coefficient of linear thermal expansion for TiN: NNP vs. MEAM [35].

Table 1

Calculated lattice constants a and c , elastic constants, Poisson's ratio ν , Young's modulus E , shear modulus G , and bulk modulus B using NNP, DFT [13,20], MEAM [35], and experiments [38].

		<u>a</u> (nm)	<u>c</u> (nm)	<u>C_{11}</u> (GPa)	<u>C_{12}</u> (GPa)	<u>C_{13}</u> (GPa)	<u>C_{33}</u> (GPa)	<u>C_{44}</u> (GPa)	<u>C_{66}</u> (GPa)
TiN	Exp. [33]	0.424		625	165			163	
	Ab initio cal.	0.425 [13]		590 [17]	145 [17]			169 [17]	
	MEAM [4]	0.424		659	150			183	
	MEAM	0.424		638	145			179	
	NNP	0.426		447	129			152	
Ti_2N	Ab initio cal.	0.495 [17]	0.303 [17]	300 [13]	214 [13]	115 [13]	442 [13]	157 [13]	137 [13]
	NNP	0.4937	0.3021	267	258	115	450	163	175
	ν		E (GPa)	G (GPa)	B (GPa)				
TiN	Exp. [33]	0.232				294 [17]			
	Ab initio cal.	0.235 [17]	466 [17]	189 [17]		320			
	MEAM [4]					309			
	MEAM	0.228	506	206		235			
Ti_2N	NNP	0.232	381	155		214 [13]			
	Ab initio cal.	0.277 [13]	287 [13]	112 [13]		217			
	NNP	0.246	332	133					

$$\alpha_L = \frac{1}{L} \frac{dL}{dT} \quad (3)$$

The coefficient of thermal expansion of bulk TiN is $9.4 \times 10^{-6} \text{ K}^{-1}$ [39].

The coefficient of linear thermal expansion predicted from the developed NNP was $8.95 \times 10^{-6} \text{ K}^{-1}$, while that from the MEAM potential was $8.53 \times 10^{-6} \text{ K}^{-1}$. NNP predicted the coefficient of thermal expansion precisely.

4. MD simulations

4.1. Mechanical property

The developed NNP was verified in the last section. Mechanical properties such as Young's modulus and tensile strength were investigated by uniaxial tensile loading. For TiN, MD simulation was used on the simulation model containing 3,000 atoms in a cube box with periodic boundary conditions. The model size was set to $30 \times 30 \times 30 \text{ \AA}$. The MEAM potential and NNP were used and compared in the simulation. The time step was set as 0.001 ps. Then, structural optimization was performed by using the conjugate gradient method, and the simulation model was relaxed at 300 K with NPT ensemble for 10 ps. Then, uniaxial strain was applied at a strain rate of $1 \times 10^{10} \text{ s}^{-1}$ with NPT ensemble along the [100], [111], and HYPERLINK "SPS:refid::bib11_bib2" [11 2] directions.

For Ti_2N , the model size was also $30 \times 30 \times 30 \text{ \AA}$, and it contained 2,100 atoms in a cube box with periodic boundary conditions. The NNP was used as the interatomic potential. The time step was set to 0.001 ps, and structural optimization was performed using the conjugate gradient method, followed by relaxation at 300 K with NPT ensemble for 10 ps. After relaxation, uniaxial strain was applied at a strain rate of $1 \times 10^{10} \text{ s}^{-1}$. Because Ti_2N has a tetragonal crystal structure, uniaxial loading was applied along the [100] and [001] directions. In addition, uniaxial loading was applied along [111] and [112]. The simulation models were created using Atomsk [40].

Table 2 shows the Young's modulus and tensile strength for the TiN and Ti_2N tensile simulations along the tensile direction. For TiN, the Young's moduli from NNP and MEAM were in good agreement, except for those in the [100] direction. For Ti_2N , the Young's moduli were similar except for those in the [100] direction. For tensile strength, NNP exhibited good agreement with the MEAM potential. The tensile strength of Ti_2N was greater than that of TiN, indicating that Ti_2N is stronger than TiN.

4.2. Fracture toughness

The fracture toughness of TiN and Ti_2N were evaluated. MD simulations of crack propagation were conducted. NNP was verified by its

Table 2

Young's modulus and tensile strength for TiN and Ti_2N along the tensile direction.

Young's modulus (GPa)			
Tensile direction	TiN MEAM	NNP	Ti_2N NNP
[100]	467	303	204
[001]			301
[111]	293	315	298
[112]	198	207	322
Tensile strength (GPa)			
Tensile direction	TiN MEAM	NNP	Ti_2N NNP
[100]	23.53	21.45	32.14
[001]			35.62
[111]	19.1	24.97	31.58
[112]	22.98	24.18	34.10

comparison with the MEAM potential for TiN, and then NNP was used to evaluate the fracture toughness of Ti_2N . Fig. 7 shows the simulation model used to simulate crack growth. The model dimensions were $6 \text{ nm} \times 8 \text{ nm} \times 2 \text{ nm}$, and there were 9,918 atoms in the TiN model and 8,064 atoms in the Ti_2N model. These simulations were performed under plane strain conditions, and the periodic condition was applied along the z-axis. Free boundary conditions were applied for the x-axis and y-axis. Then, structural relaxation with the conjugate gradient method was performed for each model, followed by relaxation at 300 K with NPT ensemble. The initial crack was created by removing interactions of both sides of cracks. Other models were created to compare crack shapes and sizes: (1) 6 Å edge crack, (2) 12 Å edge crack, (3) 6 Å central crack, and (4) 12 Å central crack (Fig. 7). Uniaxial loading was applied for the y-axis direction at a strain rate of $3 \times 10^{10} \text{ s}^{-1}$.

Fig. 8 and Fig. 9 show the snapshots of TiN and Ti_2N crack models at different simulation time points, respectively. These snapshots were recorded using Ovito [41]. Each simulation model contained a 12 Å edge crack. The initial crack grew according to time and extended along the x-axis.

Next, fracture toughness of each simulation model was estimated. The crack opening displacement (COD) at the crack tip was investigated, just before crack growth occurred in MD simulation. Fig. 10 shows the relationships between the loading time and crack growth length in the simulation model with a 12 Å central crack. Because it is difficult to define the crack start time at the atomistic scale, crack extension was defined to start when the initial crack length reached 3 Å ($\Delta a = 3 \text{ \AA}$). Once the initial crack reached 3 Å, the crack propagated rapidly (Fig. 10). This was crucial timing for crack propagation, corresponding to fracture toughness. Crack propagation started at almost the same time in the TiN model, while crack propagation in the Ti_2N model started later than the TiN model.

Fig. 11 shows the crack shape (opening displacement of the crack plane) when crack propagation started. The crack shape was plotted along the crack (i.e., r-direction). The relative opening displacements between two crack surfaces were carefully measured around the crack tip. From the COD (Fig. 11), the fracture toughness was calculated by using the displacement extrapolation method proposed by Yuuki et al. [42]. The extrapolation equation for the stress intensity factor is as follows:

$$K_I = C \lim_{r \rightarrow 0} [\delta_y(\cos Q + 2\epsilon \sin Q) + \delta_x(\sin Q - 2\epsilon \cos Q)] / \sqrt{r/2\pi} \quad (4)$$

where K_I is the stress intensity factor for mode I. C and ϵ are constants determined by the Poisson's ratio ν and the shear modulus μ . Q is a function determined by ϵ and the distance from the crack tip, and l is a representative length at the crack. These values are determined as follows:

$$C = 2\cosh(\epsilon\pi) / [(\chi_1 + 1)/\mu_1 + (\chi_2 + 1)/\mu_2] \quad (5)$$

$$Q = \epsilon \ln(r/l) \quad (6)$$

$$\chi_i = 3 - 4\nu_i \quad (7)$$

$$\epsilon = \frac{1}{2\pi} \ln \left(\frac{\frac{\chi_1}{\mu_1} + \frac{1}{\mu_2}}{\frac{\chi_2}{\mu_2} + \frac{1}{\mu_1}} \right) \quad (8)$$

Equation (4) was developed to calculate the fracture toughness at an interface. However, in this study, the fracture toughness of a homogeneous material was calculated; thus, Equations (5), (7), and (8) were calculated as $\chi_1 = \chi_2$ and $\mu_1 = \mu_2$, and Equations (6) and (8) were calculated as 0.

Table 3 shows the fracture toughness from the MD simulation and experiment. The fracture toughness values were estimated from the MD simulation using Equation (4). For TiN, NNP exhibited good agreement

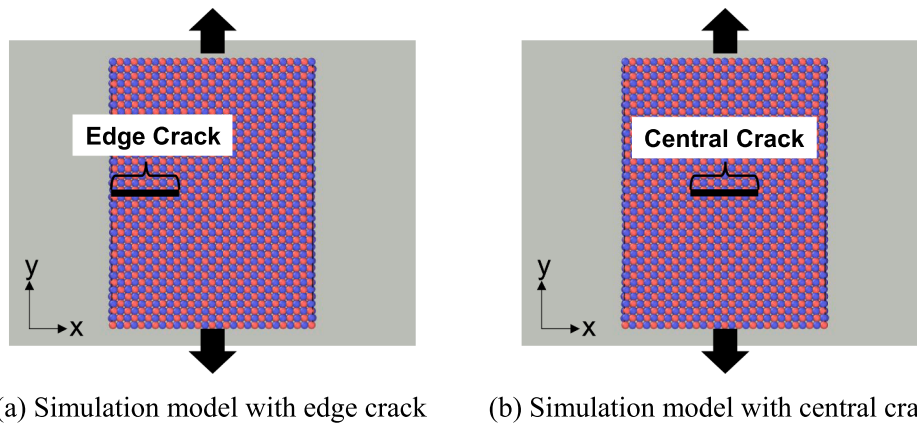


Fig. 7. MD simulation model with (a) edge crack and (b) central crack.

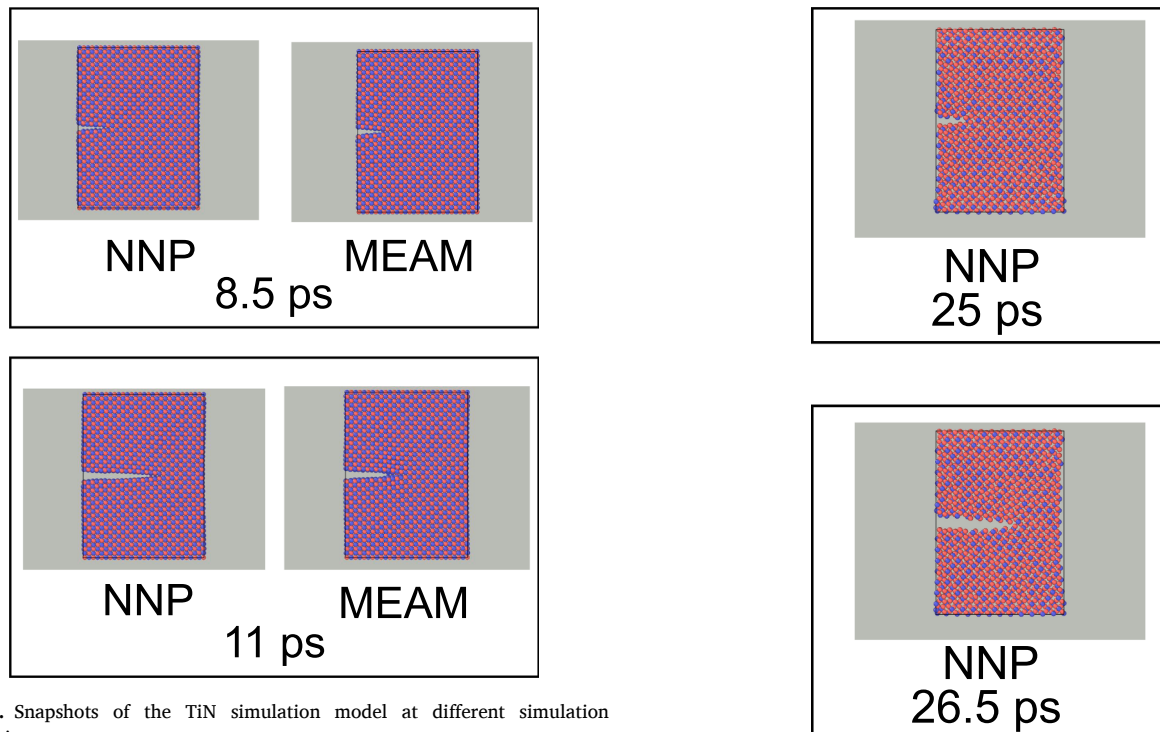


Fig. 8. Snapshots of the TiN simulation model at different simulation time points.

with the MEAM potential. The values from both interatomic potentials varied from 4.75 to $5.61 \text{ MPa}\sqrt{m}$. These values exhibited the same order of magnitude as the experimental values [43,44] in Table 3, considering the difference of scale between the experiment and MD simulation. For Ti_2N simulation models, the values varied from 2.33 to $2.62 \text{ MPa}\sqrt{m}$. The fracture toughness of Ti_2N was less than that of TiN, indicating that Ti_2N is more brittle than TiN.

5. Conclusion

This study developed an NNP for TiN and Ti_2N using the DeePMDF-kit software package. The VASP package was used to conduct AIMD simulations to comprehensively compute the relationship between atomic configurations and the corresponding total potential energies and forces on each atom, which were used to prepare the training data for the NN. Various crystalline structures of the TiN compound, as well as its amorphous form, were included in the training dataset to extend the sampling space to train a transferable model. NN training was conducted using the DeePMDF-kit software. After the training process, the resulting

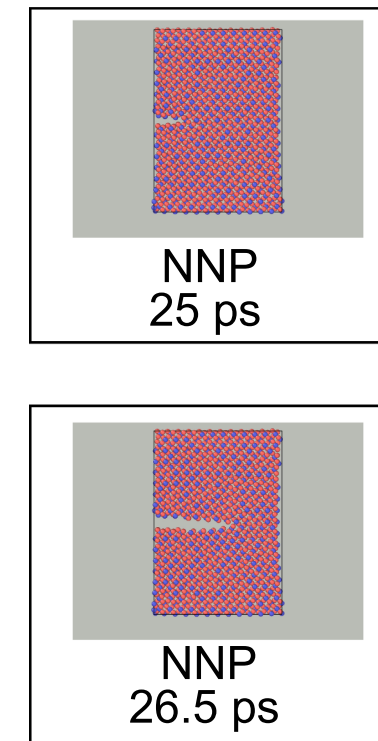


Fig. 9. Snapshots of the Ti_2N simulation model at different simulation time points.

NNP accurately predicted the energies and forces of the Ti-N system included in the training and test dataset.

The developed NNP was used in the LAMMPS package to perform MD simulations. The results revealed that the NNP can accurately reproduce the lattice constant, elastic moduli, and thermal expansion coefficients of the experiment, ab initio calculations, and MD simulations with the conventional MEAM potential. Moreover, the deformation behavior under uniaxial tension was reproduced accurately with NNP and MEAM. Finally, crack growth behavior was investigated using MD simulation due to the brittle nature of TiN; fracture toughness is a critical issue. The fracture toughness calculated by NNP was similar to that by estimated the MEAM potential. Moreover, these values exhibited the same order of magnitude with the previously reported experimental fracture toughness. As MD simulation can reproduce material deformation and fracture, the development of interatomic potentials for MD simulation is beneficial for new materials. Thus, the approach to develop new potentials using NN is extremely efficient. Finally, the NNP of Ti_2N

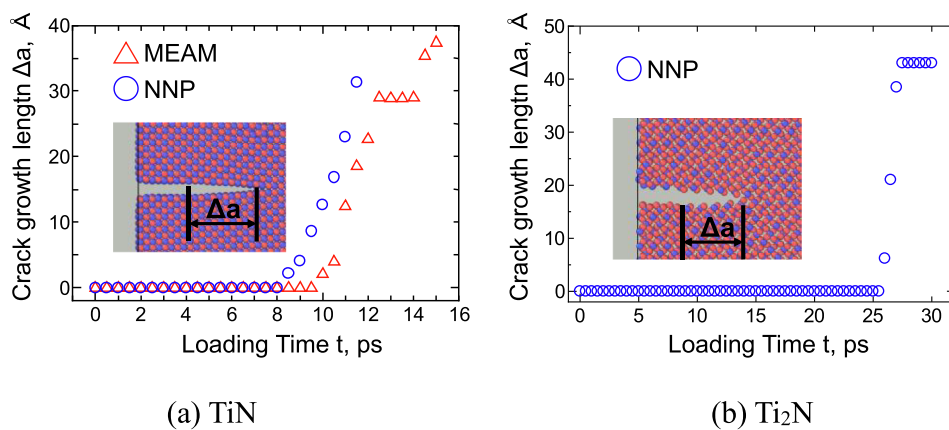


Fig. 10. Relationships between loading time and crack growth length for TiN and (b) Ti_2N simulation models.

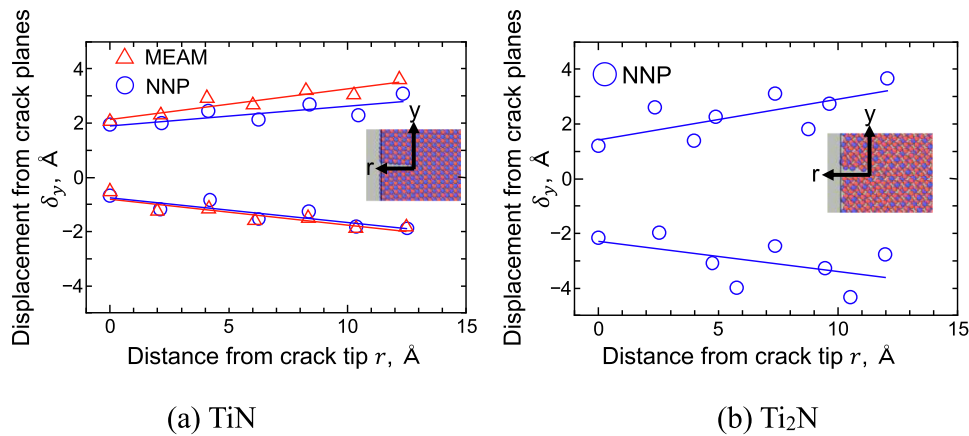


Fig. 11. Crack shape at the initiation of crack growth for TiN and (b) Ti_2N simulation models.

Table 3

Calculated fracture toughness for TiN and Ti_2N simulation models with various crack shapes.

Crack shape	TiN		Ti_2N
	MEAM	NNP	NNP
6 Å edge crack	5.09	4.75	2.33
12 Å edge crack	5.61	5.60	2.36
6 Å central crack	5.51	5.51	2.62
12 Å central crack	5.52	5.44	2.60
Experiment	2.28 [38], 2.33 [38]		-
	4.51 [39]		

was created, and its fracture toughness was examined. The fracture toughness of Ti_2N was less than that of TiN, indicating that Ti_2N is more brittle.

Declaration of Competing Interest

The authors declare that they have no known competing financial interests or personal relationships that could have appeared to influence the work reported in this paper.

Acknowledgements

This study is supported by JSPS KAKENHI (grant no. 21H01217 and 20K20966) from the Japan Society for the Promotion of Science.

References

- S. Veprek, M.G.J. Veprek-Heijman, R. Zhang, Chemistry, physics and fracture mechanics in search for superhard materials, and the origin of superhardness in nc-TiN/a-Si3N4 and related nanocomposites, *J. Phys. Chem. Solids* 68 (5) (2007), 1161–1168, <https://doi.org/10.1016/j.jpcs.2007.01.013>.
- S. Veprek, S.G. Prilliman, S.M. Clark, Elastic moduli of nc-TiN/a-Si3N4 nanocomposites: Compressible, yet superhard, *J. Phys. Chem. Solids* 71 (8) (2010) 1175–1178, <https://doi.org/10.1016/j.jpcs.2010.03.029>.
- C.K. Jin, K.H. Lee, C.G. Kang, Performance and characteristics of titanium nitride, chromium nitride, multi-coated stainless steel 304 bipolar plates fabricated through a rubber forming process, *Int. J. Hydrogen Energy* 40 (20) (2015), 6681–6688, <https://doi.org/10.1016/j.ijhydene.2015.03.080>.
- W. Aperador, J.C. Caicedo, C. Espana, G. Cabrera, C. Amaya, Bilayer period effect on corrosion-erosion resistance for [TiN/AlTiN]_n multilayered growth on AISI 1045 steel, *J. Phys. Chem. Solids* 71 (12) (2010) 1754–1759, <https://doi.org/10.1016/j.jpcs.2010.08.019>.
- H.T. Kim, M.J. Kim, S.H. Sohn, Characterization of TiN thin films grown by low-frequency (60Hz) plasma enhanced chemical vapor deposition, *J. Phys. Chem. Solids* 73 (7) (2012) 931–935, <https://doi.org/10.1016/j.jpcs.2012.02.024>.
- M. Wittmer, TiN and TaN as diffusion barriers in metallizations to silicon semiconductor devices, *Appl. Phys. Lett.* 36 (6) (1980) 456–458.
- J. Buchinger, L. Löfler, J. Ast, A. Wagner, Z. Chen, J. Michler, Z.L. Zhang, P. H. Mayrhofer, D. Holec, M. Bartosik, Fracture properties of thin film TiN at elevated temperatures, *Mater. Des.* 194 (2020) 108885, <https://doi.org/10.1016/j.materdes.2020.108885>.
- M. Stoehr, C.-S. Shin, I. Petrov, J.E. Greene, Raman scattering from TiNx ($0.67 \leq x \leq 1.00$) single crystals grown on MgO(001), *J. Appl. Phys.* 110 (8) (2011) 083503, <https://doi.org/10.1063/1.3651381>.
- K.E. Liu, X.-L. Zhou, H.-H. Chen, L.-Y. Lu, Structural and elastic properties of TiN under high pressure, *Physica B* 407 (17) (2012) 3617–3621.
- M.G. Brik, C.-G. Ma, First-principles studies of the electronic and elastic properties of metal nitrides XN (X = Sc, Ti, V, Cr, Zr, Nb), *Comput. Mater. Sci.* 51 (1) (2012) 380–388.
- E.T. Norton, C. Amato-Wierda, Kinetic and Mechanistic Studies of the Thermal Decomposition of $Ti(N(CH_3)_2)_4$ during Chemical Vapor Deposition by In Situ

- Molecular Beam Mass Spectrometry, *Chem. Mater.* 13 (12) (2001) 4655–4660, <https://doi.org/10.1021/cm0104708>.
- [12] A. Sherman, Growth and Properties of LPCVD Titanium Nitride as a Diffusion Barrier for Silicon Device Technology, *J. Electrochem. Soc.* 137 (6) (1990) 1892–1897, <https://doi.org/10.1149/1.2086826>.
- [13] S. Yu, Q. Zeng, A.R. Oganov, G. Frapper, L. Zhang, Phase stability, chemical bonding and mechanical properties of titanium nitrides: A first-principles study, *PCCP* 17 (17) (2015) 11763–11769, <https://doi.org/10.1039/c5cp00156k>.
- [14] A.R. Oganov, C.W. Glass, Crystal structure prediction using ab initio evolutionary techniques: Principles and applications, *J. Chem. Phys.* 124 (24) (2006) 244704, <https://doi.org/10.1063/1.2210932>.
- [15] A.R. Oganov, Y. Ma, A.O. Lyakhov, M. Valle, C. Gatti, Evolutionary Crystal Structure Prediction as a Method for the Discovery of Minerals and Materials, *Rev. Mineral. Geochem.* 71 (1) (2010) 271–298, <https://doi.org/10.2138/rmg.2010.71.13>.
- [16] A.R. Oganov, A.O. Lyakhov, M. Valle, How Evolutionary Crystal Structure Prediction Works—and Why, *Acc. Chem. Res.* 44 (3) (2011) 227–237, <https://doi.org/10.1021/ar1001318>.
- [17] Z. Qing-Hua, H.e. Yi-Hua, H.e. Zhao-Guo, Y. Chang, Propagation Characteristics of Whistler-Mode Chorus during Geomagnetic Activities, *Chinese Phys. Lett.* 27 (5) (2010) 055204, <https://doi.org/10.1088/0256-307X/27/5/055204>.
- [18] H. Chen, F. Peng, H.-K. Mao, G. Shen, H.-P. Liermann, Z. Li, J. Shu, Strength and elastic moduli of TiN from radial x-ray diffraction under nonhydrostatic compression up to 45 GPa, *J. Appl. Phys.* 107 (11) (2010) 113503, <https://doi.org/10.1063/1.3392848>.
- [19] B. Holmberg, M. Yhland, R. Dahlbom, J. Sjo vall, O. Theander, and H. Flood, “Structural Studies on the Titanium-Nitrogen System,” *Acta Chemica Scandinavica*, vol. 16, pp. 1255–1261, 1962.
- [20] R. Yang, C. Zhu, Q. Wei, Z. Du, Investigations on structural, elastic, thermodynamic and electronic properties of TiN, Ti₂N and Ti₃N₂ under high pressure by first-principles, *J. Phys. Chem. Solids* 98 (2016) 10–19, <https://doi.org/10.1016/j.jpcs.2016.05.012>.
- [21] J. Behler, M. Parrinello, Generalized Neural-Network Representation of High-Dimensional Potential-Energy Surfaces, *Phys. Rev. Lett.* 98 (14) (2007), <https://doi.org/10.1103/PhysRevLett.98.146401>.
- [22] X. Wang, S. Xu, W. R. Jian, X. G. Li, Y. Su, and I. J. Beyerlein, “Generalized stacking fault energies and Peierls stresses in refractory body-centered cubic metals from machine learning-based interatomic potentials,” *Computational Materials Science*, vol. 192, no. December 2020, pp. 110364–110364, 2021, doi: 10.1016/j.commatsci.2021.110364.
- [23] T. Wen, R. Wang, L. Zhu, L. Zhang, H. Wang, D.J. Srolovitz, Z. Wu, Specialising neural network potentials for accurate properties and application to the mechanical response of titanium, *NPJ Comput. Mater.* 7 (1) (2021), <https://doi.org/10.1038/s41524-021-00661-y>.
- [24] R. Kobayashi, D. Giofré, T. Junge, M. Ceriotti, W.A. Curtin, Neural network potential for Al-Mg-Si alloys, *Phys. Rev. Mater.* 1 (5) (2017), <https://doi.org/10.1103/PhysRevMaterials.1.053604>.
- [25] A. P. Thompson, L. P. Swiler, C. R. Trott, S. M. Foiles, and G. J. Tucker, “Spectral neighbor analysis method for automated generation of quantum-accurate interatomic potentials,” (in English), vol. 285, 2015-03-15 2015, doi: 10.1016/j.jcp.2014.12.018 Journal Name: *Journal of Computational Physics*; Journal Volume: 285; Journal Issue: C.
- [26] L. Zhang, J. Han, H. Wang, W. Saidi, R. Car, and W. Ee, *End-to-end Symmetry Preserving Inter-atomic Potential Energy Model for Finite and Extended Systems*. 2018.
- [27] L. Zhang, J. Han, H. Wang, R. Car, and E. Weinan, “Deep Potential Molecular Dynamics: A Scalable Model with the Accuracy of Quantum Mechanics,” *Physical Review Letters*, vol. 120, no. 14, pp. 143001–143001, 2018, doi: 10.1103/PhysRevLett.120.143001.
- [28] C. Chen, Z. Deng, R. Tran, H. Tang, I.-H. Chu, S.P. Ong, Accurate force field for molybdenum by machine learning large materials data, *Phys. Rev. Mater.* 1 (4) (2017), <https://doi.org/10.1103/PhysRevMaterials.1.043603>.
- [29] H. Wang, L. Zhang, J. Han, E. Weinan, *DeePMD-kit: A deep learning package for many-body potential energy representation and molecular dynamics*, *ArXiv* (2018) vol. [abs/1712.03641](https://arxiv.org/abs/1712.03641).
- [30] S. Plimpton, Fast Parallel Algorithms for Short-Range Molecular Dynamics, *J. Comput. Phys.* 117 (1) (1995) 1–19, <https://doi.org/10.1006/jcph.1995.1039>.
- [31] L. Tang, Z.J. Yang, T.Q. Wen, K.M. Ho, M.J. Kramer, C.Z. Wang, Development of interatomic potential for Al-Tb alloys using a deep neural network learning method, *PCCP* 22 (33) (2020) 18467–18479, <https://doi.org/10.1039/d0cp01689f>.
- [32] G. Kresse, J. Furthmüller, Efficient iterative schemes for ab initio total-energy calculations using a plane-wave basis set, *Phys. Rev. B* 54 (16) (1996) 11169–11186.
- [33] G. Kresse, J. Furthmüller, Efficiency of ab-initio total energy calculations for metals and semiconductors using a plane-wave basis set, *Comput. Mater. Sci.* 6 (1) (1996) 15–50, [https://doi.org/10.1016/0927-0256\(96\)00008-0](https://doi.org/10.1016/0927-0256(96)00008-0).
- [34] H.-S. Tsai, C.-H. Hsu, C.-C. Chi, Y.-C. Wang, F.-W. Liu, S.-Y. Tang, C.-J. Tsai, H. Ouyang, Y.-L. Chueh, J.-H. Liang, Non-layered Ti₂N synthesized by plasma process for the anodes of lithium-ion batteries, *Inorg. Chem. Front.* 6 (1) (2019) 172–175.
- [35] Y.-M. Kim, B.-J. Lee, Modified embedded-atom method interatomic potentials for the Ti-C and Ti-N binary systems, *Acta Mater.* 56 (14) (2008) 3481–3489, <https://doi.org/10.1016/j.actamat.2008.03.027>.
- [36] J.O. Andersson, T. Helander, L. Höglund, P. Shi, B. Sundman, Thermo-Calc & DICTRA, computational tools for materials science, *Calphad* 26 (2) (2002) 273–312, [https://doi.org/10.1016/S0364-5916\(02\)00037-8](https://doi.org/10.1016/S0364-5916(02)00037-8).
- [37] T. Bazhirov, *Data-centric online ecosystem for digital materials science*. 2019.
- [38] R. Ahuja, O. Eriksson, J.M. Wills, B. Johansson, Structural, elastic, and high-pressure properties of cubic TiC, Ti₂N, and TiO, *Phys. Rev. B – Condensed Matter Mater. Phys.* 53 (6) (1996) 3072–3079, <https://doi.org/10.1103/PhysRevB.53.3072>.
- [39] H. Holleck, Material selection for hard coatings, *J. Vac. Sci. Technol. A* 4 (6) (1986) 2661–2669, <https://doi.org/10.1116/1.573700>.
- [40] P. Hirrel, Atomsk: A tool for manipulating and converting atomic data files, *Comput. Phys. Commun.* 197 (2015) 212–219, <https://doi.org/10.1016/j.cpc.2015.07.012>.
- [41] A. Stukowski, Visualization and analysis of atomistic simulation data with OVITO—the Open Visualization Tool, *Modell. Simul. Mater. Sci. Eng.* 18 (1) (2010) 015012, <https://doi.org/10.1088/0965-0393/18/1/015012>.
- [42] R. Yuuki, J.-Q. Liu, J.-O. Xu, T. Ohira, T. Ono, Evaluation of the Fatigues Strength of Adhesive Joints Based on Interfacial Fracture Mechanics, *J. Soc. Mater. Sci. Japan* 41 (1992) 1299–1304.
- [43] M. Ghidelli, M. Sebastiani, K.E. Johanns, G.M. Pharr, Effects of indenter angle on micro-scale fracture toughness measurement by pillar splitting, *J. Am. Ceram. Soc.* 100 (12) (2017) 5731–5738.
- [44] W. Feng, D. Yan, J. He, G. Zhang, G. Chen, W. Gu, S. Yang, Microhardness and toughness of the TiN coating prepared by reactive plasma spraying, *Appl. Surf. Sci.* 243 (1-4) (2005) 204–213, <https://doi.org/10.1016/j.apsusc.2004.09.064>.